

# UNIG: MODELLING UNITARY 3D GAUSSIANS FOR VIEW-CONSISTENT 3D RECONSTRUCTION

**Anonymous authors**

Paper under double-blind review

## ABSTRACT

In this work, we present UniG, a view-consistent 3D reconstruction and novel view synthesis model that generates a high-fidelity representation of 3D Gaussians from sparse images. Existing 3D Gaussians-based methods usually regress Gaussians per-pixel of each view, create 3D Gaussians per view separately, and merge them through point concatenation. Such a view-independent reconstruction approach often results in a view inconsistency issue, where the predicted positions of the same 3D point from different views may have discrepancies. To address this problem, we develop a DETR (DEtection TRansformer)-like framework, which treats 3D Gaussians as decoder queries and updates their parameters layer by layer by performing multi-view cross-attention (MVDFA) over multiple input images. In this way, multiple views naturally contribute to modeling a unitary representation of 3D Gaussians, thereby making 3D reconstruction more view-consistent. Moreover, as the number of 3D Gaussians used as decoder queries is irrespective of the number of input views, allow an arbitrary number of input images without causing memory explosion. Extensive experiments validate the advantages of our approach, showcasing superior performance over existing methods quantitatively (improving PSNR by 4.2 dB when trained on Objaverse and tested on the GSO benchmark) and qualitatively.

## 1 INTRODUCTION

3D object reconstruction and novel view synthesis (NVS) are pivotal in computer vision and graphics, converting 2D images into detailed 3D structures in various applications such as robotics, augmented reality, virtual reality, medical imaging, archaeology, and more. Neural Radiance Fields (NeRF) attempts (Xu et al., 2024; Mildenhall et al., 2020; Wang et al., 2021a; Chen et al., 2021; Yu et al., 2021; Liu et al., 2024a; Xiong et al., 2024) are notable in 3D fields recently. However, their progress is impeded by slow rendering speeds due to the implicit. Recently, as a semi-implicit representation, 3D Gaussian Splatting (3D GS) (Kerbl et al., 2023) has achieved remarkable optimization speed and high-quality novel view rendering performance in representing objects or scenes.

However, many recent methods based on 3D GS techniques encounter the challenge of view inconsistency. This issue arises due to imprecise depth estimations from individual views, leading to duplicated representations of the same object regions within the 3D reconstructions from different perspectives. For instance, MVGamba (Yi et al., 2024) treats images and 3D Gaussians as sequences in Mamba (Gu & Dao, 2023; Dao & Gu, 2024) which leads to input view order induced view inconsistency. Splatter Image (Szymanowicz et al., 2024) and LGM (Tang et al., 2024a) predict pixel-aligned 3D Gaussians for each input view in the camera space of the corresponding input view. Then these 3D Gaussians are transformed from camera spaces of each view to the world space and naively merged together to obtain the ultimate 3D Gaussians, as depicted in fig. 1(a).

However, such dimension lifting from 2D images to 3D Gaussians in different views are independent and lacks interactions among different views, thus it may result in a single object point being represented by multiple 3D Gaussians at different positions, leading to the aforementioned view-inconsistency issue (Yang et al., 2024; Dong & Wang, 2024).

To address this issue, we propose a **Unitary 3D Gaussians (UniG)** representation. Inspired by Deformable DETR (Liu et al., 2023b; Li et al., 2024; Zhang et al., 2023; Liu et al., 2022; Li et al., 2023a) that treats the position and properties of bounding box (Bbox) as queries of the Transformer

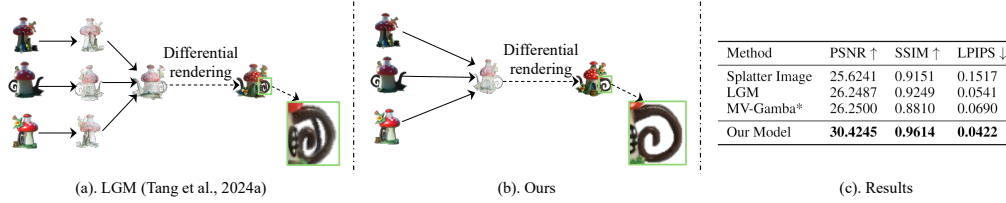


**Figure 1:** (a) Previous methods such as LGM (Tang et al., 2024a) directly concatenate Gaussians from different views, leading to view inconsistency. (b) Our method employs a unitary set of 3D Gaussians, projecting them onto each view and integrating information across views for Gaussian updates. (c) Our approach significantly surpasses previous methods in the novel view synthesis task.

decoder, we develop a DETR-like Transformer encoder-decoder framework, which treats 3D Gaussians as decoder queries and updates their parameters layer by layer by performing cross-attention over multiple input views as keys and values. To work over multi-view input, we propose a multi-view deformable attention (MVDFA) operation, where each 3D point fetches related information from multi-view 2D images simultaneously, effectively guaranteeing the consistency. More specifically, MVDFA utilize camera modulation techniques (Karras et al., 2019; Hong et al., 2024) to diversify queries based on views. The queries are linearly transformed to make difference in each view, with the weights and bias trained from camera parameters. Such operation gives each view its corresponding camera pose information. The view-specific queries are then used for performing deformable attention over corresponding images. Although similar to DFA3D (Li et al., 2023a) and BEVFormer (Li et al., 2022) in employing deformable attention in 3D with a point projection strategy, our model prioritizes multi-view distinctions (different queries in different views) to achieve a more precise 3D representation. Further elaboration is available in section 2.

As the number of 3D Gaussians is usually very large, e.g. over 10,000, the self-attention operation in a deformable Transformer decoder layer will demand a significant memory and computational cost. To improve the efficiency, inspired by (Wang et al., 2021b), we introduce a 3D Spatial Efficient Self-Attention (SESA) approach, leveraging Fast Point Sampling (FPS) (Qi et al., 2017a) to downsize the number of keys and values while preserving the number of queries. Moreover, directly regressing the positions of 3D Gaussians may lead to convergence challenges (see appendix A.4). To address this problem, we utilize a coarse-to-fine framework, where a direct lift from 2D to 3D is employed for every pixel in randomly selected input views at the coarse stage. Then, the 3D Gaussians from this stage serve as the initialization for the deformable Transformer-based refinement network, facilitating meaningful projected positions and aiding in convergence.

In summary, our contributions are as follows:

- We propose UniG, a novel 3D object reconstruction and NVS algorithm which utilizes a unitary set of 3D Gaussians as queries in deformable Transformer. Such an approach allows all input views to contribute to the same 3D representation and effectively addresses the view inconsistency issue and supports arbitrary number of input views.
- We propose to use MVDFA for tackling the multi-view fusion challenge, SESA for minimizing the memory usage in self-attention, and a coarse-to-fine framework for mitigating the convergence issue when directly regressing world coordinates of 3D Gaussians.
- Both quantitative and qualitative experiments are conducted for evaluation. Our proposed method achieves the state-of-the-art performance on the commonly-used benchmark.

## 2 RELATED WORK

**3D reconstruction from images** Recently, various methods have been explored to reconstruct detailed 3D object from limited viewpoints. (Liu et al., 2024b;c; Tang et al., 2024b; Song et al., 2021a) view the problem as an image-conditioned generation task. Leveraging pretrained generative models like Rombach et al. (2022), they achieve realistic renderings of novel views. However, diffusion models require longer time to generate 3D with multi-step denoising process, thus limiting their applicability in real-time scenarios. Recent methodologies that rely on a single forward process

for 3D reconstruction, utilizing Neural Radiance Field (NeRF) (Mildenhall et al., 2020) as a robust 3D representation, have demonstrated effective performance in the field of 3D reconstruction. (Yu et al., 2021; Cao et al., 2022; Guo et al., 2022; Lin et al., 2022; Li et al., 2023b; Müller et al., 2022; Liu et al., 2024d; Wei et al., 2024; Tochilkin et al., 2024; Xu et al., 2024; Yu et al., 2021; Wang et al., 2021a; Chen et al., 2021). However, due to the slow rendering speed of NeRF, it is being supplanted by a new, super-fast, semi-implicit representation—3D Gaussian Splatting (3D GS) (Kerbl et al., 2023). Triplane-Gaussian (Zou et al., 2024), Gamba (Shen et al., 2024), and DIG3D (Wu et al., 2024) make promising results on single image 3D reconstruction. To expand the application of 3D Gaussian Splatting to multi-view situation, SplatterImage (Szymanowicz et al., 2024), LGM (Tang et al., 2024a), pixelSplat (Charatan et al., 2024), MVSplat (Chen, Yuedong and Xu, Haoifei and Zheng, Chuanxia and Zhuang, Bohan and Pollefeys, Marc and Geiger, Andreas and Cham, Tat-Jen and Cai, Jianfei, 2024), based on 3D Gaussian Splatting, typically handle each input view independently and naively concatenate the resulting 3D Gaussian assets from each view. This method suffers from a lack of information exchange among different views, resulting in inefficient utilization of 3D Gaussians and being view inconsistency. GS-LRM (Zhang et al., 2024) and GRM (grm, 2024) take the similar model structure comparing to LGM while still handle each input view independently, theoretically having the view inconsistency problem because they first predict 3D Gaussians in each camera space and then naively merge them in world space, as the depth of the predicted 3D Gaussians in each view would always have errors, which will inevitably lead to the misaligned 3D Gaussians merged in the world space. Furthermore, these methods are unable to accommodate an arbitrary number of views as input.

**Deformable Transformer in 3D** DFA3D (Li et al., 2023a) and BEVFormer (Li et al., 2022) are introduced to address the feature-lifting challenge in 3D detection and autonomous driving tasks. They achieve notable performance enhancements by employing a deformable Transformer to bridge the gap between 2D and 3D. DFA3D initially uses estimated depth to convert 2D feature maps to 3D, sampling around reference points for deformable attention in each view. However, the 3D sampling point design causes all projected 2D points to represent a singular point, neglecting view variations. BEVFormer (Li et al., 2022) regards the Bird’s-Eye-View (BEV) features as queries, projecting the feature onto each input view. The Spatial Cross-Attention facilitates the fusion of BEV and image spaces, though challenges persist sampling 4 height values per pillar in the BEV feature for selecting 3D reference points may limit coverage, posing challenges in accurate keypoint selection for the model. When contrasting DFA3D and BEVFormer with our MVDFA, a commonality lies in projecting onto 3D regression targets to extract data from various image perspectives. However, our model diverges by employing camera modulation to differentiate queries across views, enabling more specific information retrieval.

### 3 METHODS

#### 3.1 PRELIMINARIES OF 3D GS

3D GS (Kerbl et al., 2023) is a novel rendering method that can be viewed as an extension of point-based rendering methods (Kerbl et al., 2023; Chen & Wang, 2024). Hence, 3D Gaussians can serve as effective 3D representations for efficient differentiable rendering. Each 3D Gaussian ellipsoid can be described by  $\mathbf{G} = \{\text{SH}, \boldsymbol{\mu}, \boldsymbol{\sigma}, \mathbf{R}, \mathbf{S}\}$ . The color of 3D Gaussians is represented by spherical harmonics ( $\text{SH} \in \mathbb{R}^{12}$ ) while the geometry is described by the center positions  $\boldsymbol{\mu} \in \mathbb{R}^3$ , shapes (covariance matrix  $\boldsymbol{\Sigma}$ ), and opacity ( $\sigma \in \mathbb{R}$ ) of ellipsoids (Zwicker et al., 2001; Kerbl et al., 2023). Especially, the covariance matrix can be optimized through a combination of rotation and scaling for each ellipsoid as  $\boldsymbol{\Sigma} = \mathbf{R}\mathbf{S}\mathbf{S}^T\mathbf{R}^T$ , where  $\mathbf{R} \in \mathbb{R}^4$  (represented by quaternion) represents the rotation and  $\mathbf{S} \in \mathbb{R}^3$  contains the scales in three directions.

#### 3.2 OUR METHOD

**Overall framework** As illustrated in fig. 2, our model follows an encoder-decoder framework in a coarse-to-fine manner. We employ unitary 3D Gaussian representation, which define a unitary set of 3D Gaussians in the world space no matter how many input views are given. During the coarse stage, one or more images are randomly selected as input for a simple encoder-only model to directly predict 3D Gaussians, supervised by a RGB loss. Subsequently, in the refinement network, all input

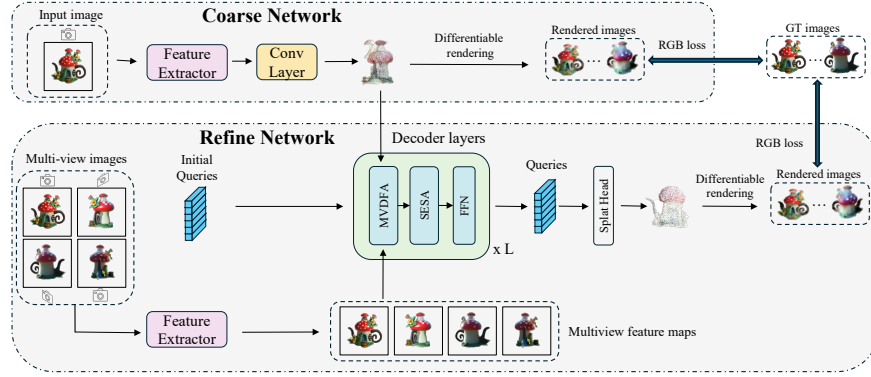


**Figure 2:** Overall Framework: In the coarse stage, 3D Gaussians are produced for each pixel of the sampled random views from the input data. In the refinement stage, 3D Gaussians from the coarse stage serves as the initialization for the refinement network. Multi-view features extracted by the feature extractor serves as keys and values of decoder. Queries are updated by the decoder layer with image features and the positions of the centers of 3D Gaussians. The final 3D Gaussian representation is regressed from the queries. MVDFA: multi-view deformable attention in section 3.2.2. SESA: spatial efficient self-attention in section 3.2.3. FFN: feed-forward network.

images undergo processing through an image encoder and a cross-view attention module to extract multi-view image features (section 3.2.1).

Each 3D Gaussian is then projected onto each view to query relevant features and update their respective parameters by query refinement decoder with multi-view deformable attention (MVDFA)(section 3.2.2). Spatially efficient self-attention is utilized to reduce computational and memory costs, enabling the utilization of more 3D Gaussians for object reconstruction (section 3.2.3). Moreover, the coarse-to-fine design aims to ensure that the initial positions of the center of 3D Gaussians are not too distant from the ground truth or outside the field of view to guarantee the training convergence (section 3.2.4). The training objective is detailed in section 3.2.5.

### 3.2.1 FEATURE EXTRACTOR

To extract image features from multi-view input, we utilize UNet (Ronneberger et al., 2015; Song et al., 2021b), a widely employed feature extractor in 3D reconstruction tasks, as demonstrated in Tang et al. (2024a); Szymanowicz et al. (2024). To enhance the network’s understanding of the complete 3D object, multi-view cross-attention is employed to transfer information among views right after the UNet block, activated when the number of input views exceeds one. In this configuration, each input view acts as queries, while the concatenation (post-flattening) of the remaining views serves as keys and values. To efficiently enable cross-attention across all views, we employ shifted-window attention, as introduced in the Swin Transformer (Liu et al., 2021). This mechanism reduces interactions by focusing on tokens within a local window, effectively reducing memory usage for large input sequences. By processing tokens within a fixed window, shifted-window attention effectively lowers the computational complexity, thereby enhancing the overall efficiency.

### 3.2.2 VIEW-AWARE QUERY REFINEMENT DECODER

**Decoder structure** In the decoder module, we employ a fixed number of queries  $\mathbf{Q} \in \mathbb{R}^{N \times C}$  with  $N$  and  $C$  denote the number of Gaussians and the hidden dimension to model 3D Gaussians by associating queries with 3D Gaussian ellipsoid parameters  $\mathbf{G}$ , including the center  $\mu$ , opacity  $\sigma$ , rotation  $\mathbf{R}$ , scaling  $\mathbf{S}$ , and Spherical Harmonics  $\mathbf{SH}$ . As depicted in fig. 2, the queries navigate through multiple decoder layers, each including a multi-view deformable attention (MVDFA) (section 3.2.2) mechanism to leverage image features, a spatial efficient self-attention (SESA) (section 3.2.3) layer for inter-Gaussian interactions, and a feed-forward network (FFN). The functionality of a decoder layer can be summarized by eq. (1), where  $\mathbf{F}$  represents image features from different views and  $\mathbf{P}^l$



signifies reference points in the  $l$ -th layer.

$$\mathbf{Q}^{l+1} = \text{FFN}(\text{SESA}(\text{MVDFA}(\mathbf{Q}^l, \mathbf{P}^l, \mathbf{F}))) \quad (1)$$

Finally, queries are processed through a splatter head  $\mathcal{S}$  to compute  $\Delta \mathbf{G} = \mathcal{S}(\mathbf{Q})$  for updating the 3D Gaussian parameters:  $\mathbf{G}' = \mathbf{G} + \Delta \mathbf{G}$  (except for rotation, which is updated by multiplication). Here, all views contribute to unitary 3D Gaussians, emphasizing the most relevant features. This strategy effectively alleviates the view inconsistency issue and is computationally more efficient.

**Multi-view deformable attention (MVDFA)** The goal of MVDFA is to enhance the unified queries and Gaussian representations by integrating multi-view image features. Following original design of DFA, trainable sampling points are employed on the image features to sample the most relevant image features as values (Carion et al., 2020; Zhu et al., 2021). The remaining problem lies in determining the sampling points and attention scores. Specifically, we project the 3D queries onto each image view and adjust it using camera modulation to account for view discrepancies. The sampling offsets and attention scores are subsequently obtained from the view-specific queries.

By leveraging the center  $\boldsymbol{\mu}$  of each 3D Gaussian from the previous layer, along with the corresponding camera poses  $\pi_i$  and intrinsic parameters  $K_i$  for the  $i$ -th image, we can compute UV coordinates  $\mathbf{P}_i$  by projecting the center coordinates of each 3D Gaussian onto the image plane of the  $i$ -th input image using the pinhole camera model (Forsyth & Ponce, 2003; Hartley & Zisserman, 2003):  $\mathbf{P}_i = K_i \pi_i \boldsymbol{\mu}$ . In this context, both matrices  $K_i$  and  $\pi_i$  are expressed in homogeneous form. These UV coordinates in  $\mathbf{P}_i$  then function as the reference points for 2D deformable attention.

As depicted fig. 3 (a), in 3D, we have a set of queries associated with 3D Gaussian parameters  $\mathbf{G}$  while the queries for each image planes should to be adjusted to suit each view individually. To tackle this issue, we start by using camera modulation with the adaptive layer norm (adaLN) (Hong et al., 2024; Karras et al., 2019; 2020; Viazovetskyi et al., 2020) to generate view-specific queries. More information on this modulation is provided in fig. 3(b). Subsequently, a linear layer to predicts the sampling offsets  $\Delta \mathbf{s}$  for retrieving images features as values and another linear layer to predicts the attention scores  $\alpha$  of the sampling points  $\mathbf{s}$ . Following (Zhang et al., 2023; Zhu et al., 2021), we compute attention scores directly from queries, omitting keys to streamline calculations. Then, we apply the grid sampling algorithm with bilinear interpolation to extract image features at these sampling points, which act as the values  $\mathbf{v}$  for cross attention.

Finally, for each input view, we compute the updated queries for each view using the attention scores  $\alpha$  and sampled values  $\mathbf{v}$ . The ultimate unitary queries are then computed as a weighted sum of individual view queries, with the weights calculated using an linear layer on the view-specific queries. Detailed pseudo code for our multi-view deformable cross-attention is available in fig. 3(b).

### 3.2.3 SPATIAL EFFICIENT SELF-ATTENTION (SESA)

Our multi-view deformable cross-attention mechanism demonstrates a superior efficiency in terms of computational cost and memory usage. However, self-attention is computationally expensive, especially with numerous 3D Gaussians. Updating each Gaussian with information from all others may not always be essential, as neighboring Gaussians often contain similar information. To tackle this problem, drawing inspiration from Wang et al. (2021b), we introduce a method to reduce the number of keys and values while keeping the number of queries unchanged during self-attention. This selective update strategy enables each query to be updated with a subset of related queries, effectively enhancing the information exchange efficiency. To ensure crucial information flow, we leverage the Fast Point Sampling (FPS) algorithm from point cloud methodologies (Qi et al., 2017a;b). By utilizing Gaussian centers  $\boldsymbol{\mu}$  to identify distant points for querying, we optimize memory usage while guaranteeing essential information sharing among Gaussians. Additional details are in appendix A.1.

### 3.2.4 COARSE-TO-FINE MODEL

**Locating Gaussian centers in the world space** In Szymanowicz et al. (2024), the Gaussian centers are located in each input view’s camera space, i.e.  $\boldsymbol{\mu}_{\text{cam}} = [x_{\text{cam}}, y_{\text{cam}}, z_{\text{cam}}] = [u_1 d + \Delta_x, u_2 d + \Delta_y, d + \Delta_z]$ , where the center coordinates  $x_{\text{cam}}, y_{\text{cam}}, z_{\text{cam}}$  are parameterized by the depth  $d$  and offset values  $(\Delta_x, \Delta_y, \Delta_z)$ . The depth  $d$  represents the length of a ray originating from the camera

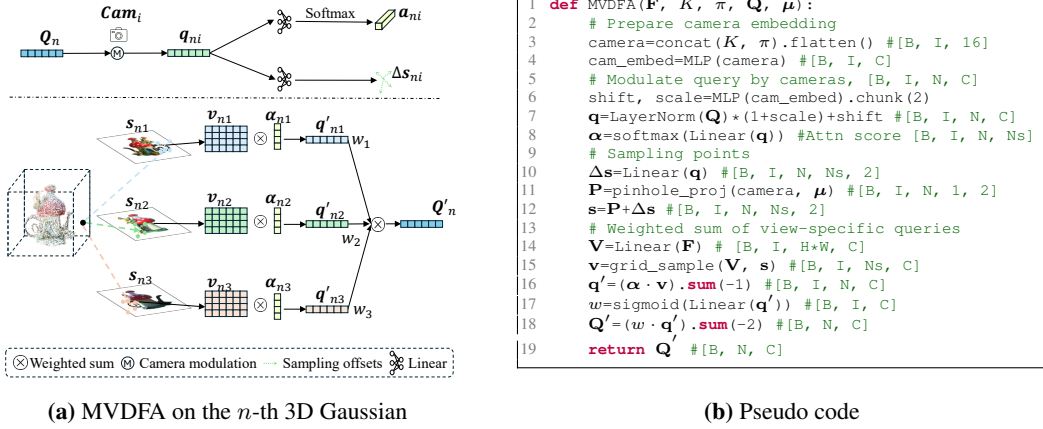


**Figure 3: MV DFA:**  $Q_n$  denotes the  $n$ -th unitary queries while  $q_{ni}$  denotes the  $n$ -th query on the  $i$ -th view modulated by the  $i$ -th camera  $Cam_i$ . Linear layers are used on  $q_{ni}$  to compute the sampling offsets  $\Delta s_{ni}$  and attention score  $\alpha_{ni}$ . The  $n$ -th 3D Gaussian is projected onto images, and surrounding sampling points  $s_{ni} = P_{ni} + \Delta s_{ni}$  are sampled using offsets  $\Delta s_{ni}$ . Values  $v_{ni}$  are image features sampled at  $s_{ni}$ . The final query is calculated by the weighted sum of updated view-specific queries  $q'_{ni}$ , where  $w_i$  is the weight calculated by a linear layer on  $q'_{ni}$ .  $B$  is batch size,  $I$  is the number of views,  $C$  is the hidden dimension,  $N$  is the number of Gaussians, *pinhole\_proj* is the projection from 3D to 2D with the pinhole model.  $F$  is the image feature with height  $H$  and weight  $W$ .  $K$  and  $\pi$  are camera intrinsics and extrinsics, respectively.

center.  $u_1, u_2$  are the UV coordinates of the ray passing through the corresponding input image. This design represents each point with multiple Gaussians, potentially introducing view inconsistency due to concatenation issues at various points caused by depth inaccuracies and tend to shortcut input views (Wu et al., 2024). In our framework, we define unitary Gaussians in the world space, project their centers to each input view for feature retrieval, as depicted in fig. 3(a). The centers of Gaussians can be written as  $\mu_{world} = [x_{world}, y_{world}, z_{world}]$ . However, during the initial training phases, discrepancies between the 3D Gaussian centers and ground truth often result in imprecise selection of image features at sampling points, presenting challenges for model convergence.

We employ a relative coordinate system, where the camera poses for all views are known. The initial input view is established as the world coordinates (with the camera pose represented by the identity matrix), and subsequently, all other views are transformed to align with these coordinates. This approach allows us to represent all 3D data within this consistent relative coordinate system.

**Coarse-to-fine** To address this issue, we utilize a coarse network that directly regress 3D Gaussian parameters with one or more randomly selected input images as input. The role of this network is to provide a coarse initialization of 3D Gaussians for the subsequent refinement network. We use the UNet architecture as the feature extractor to train the coarse network. Subsequently, we use this trained parameters to initialize the refinement stage and independently train the refinement network.

### 3.2.5 TRAINING OBJECTIVE

Building upon prior 3D Gaussian-based reconstruction approaches, we leverage the differentiable rendering implementation by Kerbl et al. (2023) to generate RGB images from the 3D Gaussians produced by our model. For each object, we render 4 input views and 8 additional views (12 views in total) for supervision. Furthermore, aligning with the methodologies ((Hong et al., 2024; Tang et al., 2024a)), we employ a RGB loss in eq. (2), which consists of both a mean square error loss  $\mathcal{L}_{MSE}$  and a VGG-based LPIPS (Learned Perceptual Image Patch Similarity) loss (Zhang et al., 2018a)  $\mathcal{L}_{LPIPS}$  to guide the rendered views. Here  $I_{pd}$  represents the rendered views supervised by the ground truth images  $I_{gt}$ .

$$\mathcal{L} = \mathcal{L}_{MSE}(I_{pd}, I_{gt}) + \lambda \mathcal{L}_{LPIPS}(I_{pd}, I_{gt}) \quad (2)$$

## 4 EXPERIMENTS

This section delves into experiment details and outcomes. In section 4.1, we give dataset specifics, evaluation metrics, and implementation details. section 4.2 delves into quantitative and qualitative results for sparse view novel view synthesis, along with the visualization of 3D Gaussian centers as a point cloud. section 4.3 provides a comparative analysis of processing speeds and memory costs. section 4.4 presents an ablation study. Lastly, The versatility of our model extends to tasks such as image-to-3D and text-to-3D generation using a diffusion model, detailed in section 4.5.

### 4.1 DATASET AND EXPERIMENT SETTINGS

**Dataset** We utilized a refined subset of the Objaverse LVIS dataset (Deitke et al., 2023) for training and validation. The training dataset comprised two sets of rendered images: one set featured 12 random camera poses, while the other included input rendering images captured from fixed view-points (front, back, left, right). Supervision was provided from 32 random views spanning elevations between -30 to 30 degrees. The resolution of the rendered images was downscaled to  $128 \times 128$ .

To evaluate our model, we conducted tests on the Google Scanned Objects (GSO) benchmark. Two test sets were utilized: one with fixed-view inputs (e.g., front, left, back, right) at 0 degrees elevation, tested on 32 random views with elevations ranging from 0 to 30 degrees, and the other includes 25 random views with corresponding camera poses. Importantly, there are no constraints on the elevation of the rendered views. We refer to these test sets as GSO-random and GSO-fixed in our subsequent analysis. More details for dataset can be found in appendix A.2.

**Evaluation metric** We compute the peak signal-to-noise ratio (PSNR), structural similarity index (SSIM) (Wang et al., 2004), and perceptual distance (LPIPS) (Zhang et al., 2018b) between the rendered images and the ground truth. Additionally, we offer visual representations of both the rendered images and the 3D Gaussian centers as a point cloud. More details are provided in appendix A.2.

### 4.2 COMPARISON WITH STATE-OF-THE-ART METHODS

We provide the comparison with the state-of-the-art methods in this section.

#### 4.2.1 FIXED VIEW INPUT

Table 1: Quantitative results for inputting 4 views on GSO-fixed dataset. \*The results of MV-Gamba are cited from the paper as they do not provide code or a test set.

Method	PSNR $\uparrow$	SSIM $\uparrow$	LPIPS $\downarrow$
Splatter Image (Szymanowicz et al., 2024)	25.6241	0.9151	0.1517
LGM (Small) (Tang et al., 2024a)	17.4810	0.7829	0.2180
LGM (Large) (Tang et al., 2024a)	26.2487	0.9249	0.0541
InstantMesh (Xu et al., 2024)	23.0177	0.8893	0.0886
MV-Gamba* (Yi et al., 2024)	26.2500	0.8810	0.0690
Our Model	<b>30.4245</b>	<b>0.9614</b>	<b>0.0422</b>

We evaluated recent multi-view reconstruction models using 4 views as input. Splatter Image (Szymanowicz et al., 2024) were trained with their native data loaders, adjusting inputs to 4 views and supervision to 12. LGM and InstantMesh were evaluated using the provided checkpoints, with “Small” indicating models tailored to 128 resolution and “Large” to 256 resolution. All models were assessed assuming the same number of training views.

table 1 showcases the performance of these methods in novel view synthesis using 4 fixed views (front, back, right, left) on the GSO-fixed dataset. Our model surpassed previous approaches in PSNR, SSIM, and LPIPS for novel view synthesis, with a significant improvement of approximately 4.2 dB in PSNR. Additional results for 6 and 8 view inputs are available in appendix A.3.2.

We present visualization results for novel view synthesis in fig. 4 and 3D Gaussian centers represented as point clouds in appendix A.3.1. In our experiments, with resolution of 128, the LGM model corresponds to the small version. Observations in the figures reveal view inconsistency in LGM and a lack of details in InstantMesh, whereas our model maintains both details and view consistency. Further visualizations at a resolution of 256 are accessible in appendix A.3.1.

#### 4.2.2 RANDOM VIEW INPUT

Table 2: Quantitative results for inputting 4 views on GSO-random dataset.

Method	PSNR $\uparrow$	SSIM $\uparrow$	LPIPS $\downarrow$
Splatter Image	25.7660	0.8932	0.2575
LGM	15.1113	0.8440	0.1592
InstantMesh	17.3073	0.8525	0.1376
Our Model	<b>26.3020</b>	<b>0.9255</b>	<b>0.0836</b>

not reduced much, its SSIM and LPIPS reduced significantly. We provide more visualization in appendix A.3.1 fig. 14.

#### 4.2.3 INFERENCE ON ARBITRARY NUMBER OF VIEWS

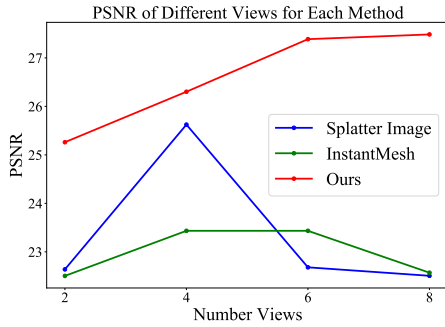


Figure 5: Quantitative results with random number of views as input. The model is trained with 4 random input views and tested with variate number of views.

While other methods demonstrate satisfactory performance with 4 views during inference, their effectiveness diminishes as the view count deviates from 4. In contrast, our model excels as the number of views increases. It is important to highlight that LGM is not part of this comparison due to its incapacity to handle variations in the number of views between the training and testing phases.

#### 4.3 INFERENCE TIME AND MEMORY COST

Table 3: Inference time comparison. 3D: forward time, render: rendering time, inference: time of one forward and 32 rendering. Unit in seconds.

Method	3D $\downarrow$	Render $\downarrow$	Inference $\downarrow$
DreamGaussian	118.3245	0.0038	118.4461
InstantMesh	<b>0.6049</b>	0.6206	20.4641
LGM	1.6263	0.0090	1.9143
Our Model	0.6939	<b>0.0019</b>	<b>0.7538</b>

Previous methods (LGM and InstantMesh) usually rely on fixed views as input, as they align well with views generated from diffusion models like ImageDream (Wang & Shi, 2023). In real-world scenarios, users are more inclined to provide random views as input. table 2 displays the results when utilizing random 4 views as input on the GSO-random dataset. Notably, there is a performance drop observed in LGM and InstantMesh with random input views. appendix A.3.1 provides the visualization results. For Splatter Image, although the PSNR does

Training costs for 3D methods are considerable, often requiring 32 NVIDIA A100 (80G) GPUs over multiple days. Additionally, memory costs for previous methods increase linearly with the number of views, presenting challenges for training models with varying input views. Therefore, a model supporting inference with any number of inputs while being trained on a fixed set, such as 4 views, would provide significant advantages.

Our model retains unitary 3D Gaussians in world coordinates, treating views as complementary sources without compromising overall 3D integrity. This enables adaptability to variable view counts during inference, despite training on a fixed number of views. fig. 5 showcases the results of training the model with 4 random views and testing it with different number of views. More views results are in appendix A.3.2 fig. 17.

We performed inference time tests across different model types, including a diffusion-based method (DreamGaussian (Tang et al., 2024b)), a NeRF-based model (InstantMesh (Xu et al., 2024)), a previous Gaussian-based model (LGM (Tang et al., 2024a)), and our model, as detailed in table 3. Our model maintains a reduced number of Gaussians and achieves the fastest rendering speed.

In contrast to previous methods that compute 3D Gaussians per pixel per input view, our model retains a single 3D Gaussian irrespective

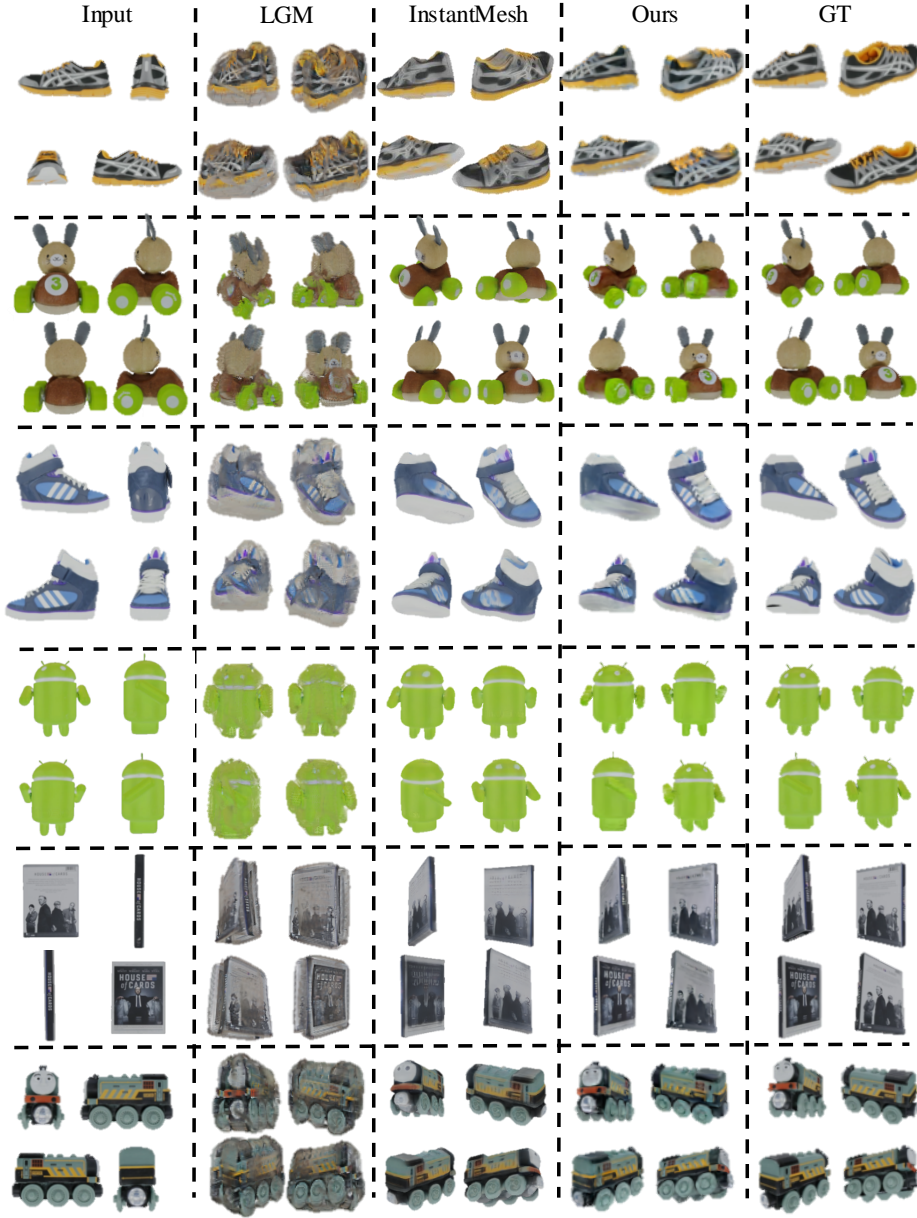


**Figure 4:** Novel views on GSO-fixed dataset for inputting 4 views with resolution 128.

of the number of views. While conventional methods exhibit linear memory expansion with additional views or higher image resolutions, our approach sustains a consistent memory overhead or experiences slight increments due to the marginally higher cost of the image feature extractor. This design theoretically enables our model to accommodate more input views and higher resolutions for enhanced outcomes, potentially circumventing the out-of-memory limitations encountered by other methods.

#### 4.4 ABLATION STUDIES

table 4 illustrates an ablation study that evaluates different components of the model architecture. All the experiments are evaluated on the Objaverse validation dataset. Removing the coarse stage and initializing randomly (without any constraint) results in the lowest performance. This problem arises from utilizing image features around the projected 3D Gaussian center within each image view, po-

tentially causing zero features and steep gradients when projections extend beyond the image plane. When the coarse stage is randomly initialized within the cone of vision (CoV), performance improves. To provide a more meaningful initialization, we incorporate a coarse stage to acquire the approximate Gaussian locations, followed by a refinement stage. This refined initialization empowers our model to achieve superior performance. Moreover, removing cross-view attention leads to a moderate decrease in performance compared to the full model. Using only the coarse stage (UNet-based) slightly underperforms the full model. Furthermore, removing the camera modulation on queries or use 3D sampling points instead of sampling on each view adversely impacts the results, underscoring the critical significance of this view-specific design. The full model achieves the best performance across all metrics, indicating that each component contributes positively to the overall model effectiveness. Additionally, we offer details on hyperparameter selections in appendix A.4.

Table 4: Ablation study on model design.

Method	PSNR $\uparrow$	SSIM $\uparrow$	LPIPS $\downarrow$
w/o coarse (ran. init.)	12.1213	0.6531	0.6224
w/o coarse (ran. init. in CoV)	22.6740	0.8711	0.2383
w/o cross view attention	25.3923	0.9013	0.1007
coarse stage only (UNet)	25.6033	0.9107	0.0930
w/o camera modulation	26.1328	0.9201	0.0883
3D sampling points	25.8392	0.9117	0.0945
Full model	<b>26.5334</b>	<b>0.9344</b>	<b>0.0667</b>

mance (fig. 16, table 6)

#### 4.5 APPLICATIONS IN 3D GENERATION

**Image-to-3D** conversion represents a fundamental application in 3D generation. Following the methodology of LGM and InstantMesh (Tang et al., 2024a; Xu et al., 2024), we initially leverage a multi-view diffusion model, ImageDream (Wang & Shi, 2023), to generate four predetermined views. Subsequently, our model is utilized for 3D Gaussian reconstruction. A comparative analysis with LGM and InstantMesh is detailed in appendix A.3.2. We also showcase the quality results of our model on both the GSO dataset and in-the-wild images in appendix A.3.1.

Our model can also do the **Text-to-3D** task. To evaluate quality, we utilize MVDream (Shi et al., 2024) to generate a single image from a text prompt. Subsequently, a diffusion model is employed to produce multi-view images, which are then processed by our model to derive a 3D representation. A qualitative comparison of the text-to-3D generation is presented in appendix A.3.1.

## 5 CONCLUSION AND LIMITATION

In this paper, we have introduced a novel sparse view 3D reconstruction and novel view synthesis method. Initially, a fixed number of 3D Gaussians with predefined properties are initialized, and each Gaussian ellipsoid is projected onto input image features extracted by a feature extractor. We propose the MVDFA block to integrate image features surrounding the projected 3D Gaussians from each view to refine the 3D Gaussians, employing a coarse-to-fine strategy to ensure robust model convergence. Additionally, we develop a spatially efficient self-attention mechanism to minimize computational costs, tackling view inconsistency and computational inefficiency. Our model accommodates an arbitrary number of views as input and showcases its effectiveness through quantitative and qualitative experiments compared to state-of-the-art methods trained on Objaverse and tested on the GSO dataset. Furthermore, with the aid of an off-the-shelf diffusion model, our model undertakes generation tasks such as image-to-3D and text-to-3D conversions. We present an ablation study elucidating the significance of each model component. While our model signifies a notable advancement in sparse view 3D reconstruction, there are inherent **limitations**. Presently, user-provided camera parameters, both camera poses and intrinsics, are necessary for projecting 3D Gaussians onto images, presenting potential challenges in 3D reconstruction. Addressing this issue stands as a focal point for future research.

Moreover, we add the ablation study on the number of views or different views input in the coarse stage in appendix A.4 table 9. We also give more view inconsistency visualization problem by visualize center of Gaussians from each view in different colors, as shown in fig. 7. Furthermore, removing the background use masks for Splatter Image and LGM may slightly improve the perfor-

## REFERENCES

- GRM: Large Gaussian Reconstruction Model for Efficient 3D Reconstruction and Generation, author=Xu Yinghao and Shi Zifan and Yifan Wang and Chen Hansheng and Yang Ceyuan and Peng Sida and Shen Yujun and Wetzstein Gordon, 2024.
- Ang Cao, Chris Rockwell, and Justin Johnson. FWD: Real-time novel view synthesis with forward warping and depth. In Proceedings of the IEEE/CVF Conference on Computer Vision and Pattern Recognition (CVPR), pp. 15713–15724, 2022.
- Nicolas Carion, Francisco Massa, Gabriel Synnaeve, Nicolas Usunier, Alexander Kirillov, and Sergey Zagoruyko. End-to-end object detection with transformers. In European conference on computer vision (ECCV), 2020.
- David Charatan, Sizhe Lester Li, Andrea Tagliasacchi, and Vincent Sitzmann. pixelsplat: 3d gaussian splats from image pairs for scalable generalizable 3d reconstruction. In Proceedings of the IEEE/CVF Conference on Computer Vision and Pattern Recognition, pp. 19457–19467, 2024.
- Anpei Chen, Zexiang Xu, Fuqiang Zhao, Xiaoshuai Zhang, Fanbo Xiang, Jingyi Yu, and Hao Su. MVSNeRF: Fast Generalizable Radiance Field Reconstruction from Multi-View Stereo. In 2021 IEEE/CVF International Conference on Computer Vision (ICCV), Oct 2021. doi: 10.1109/iccv48922.2021.01386. URL <http://dx.doi.org/10.1109/iccv48922.2021.01386>.
- Guikun Chen and Wenguan Wang. A Survey on 3D Gaussian Splatting. ArXiv, 2024.
- Chen, Yuedong and Xu, Haofei and Zheng, Chuanxia and Zhuang, Bohan and Pollefeys, Marc and Geiger, Andreas and Cham, Tat-Jen and Cai, Jianfei. Mvsplat: Efficient 3d gaussian splatting from sparse multi-view images. European Conference on Computer Vision, 2024.
- Tri Dao and Albert Gu. Transformers are SSMs: Generalized Models and Efficient Algorithms Through Structured State Space Duality. In International Conference on Machine Learning (ICML), 2024.
- Matt Deitke, Dustin Schwenk, Jordi Salvador, Luca Weihs, Oscar Michel, Eli VanderBilt, Ludwig Schmidt, Kiana Ehsani, Aniruddha Kembhavi, and Ali Farhadi. Objaverse: A universe of annotated 3d objects. In Proceedings of the IEEE/CVF Conference on Computer Vision and Pattern Recognition (CVPR), pp. 13142–13153, 2023.
- Jiahua Dong and Yu-Xiong Wang. Vica-nerf: View-consistency-aware 3d editing of neural radiance fields. Advances in Neural Information Processing Systems (NIPS), 36, 2024.
- Laura Downs, Anthony Francis, Nate Koenig, Brandon Kinman, Ryan Hickman, Krista Reymann, Thomas B McHugh, and Vincent Vanhoucke. Google scanned objects: A high-quality dataset of 3d scanned household items. In 2022 International Conference on Robotics and Automation (ICRA), pp. 2553–2560. IEEE, 2022.
- David A Forsyth and Jean Ponce. A Modern Approach. Computer vision: a modern approach, 17: 21–48, 2003.
- Albert Gu and Tri Dao. Mamba: Linear-Time Sequence Modeling with Selective State Spaces. arXiv preprint arXiv:2312.00752, 2023.
- Pengsheng Guo, Miguel Angel Bautista, Alex Colburn, Liang Yang, Daniel Ulbricht, Joshua M. Susskind, and Qi Shan. Fast and Explicit Neural View Synthesis. In 2022 IEEE/CVF Winter Conference on Applications of Computer Vision (WACV), Jan 2022. doi: 10.1109/wacv51458.2022.00009. URL <http://dx.doi.org/10.1109/wacv51458.2022.00009>.
- Richard Hartley and Andrew Zisserman. Multiple View Geometry in Computer Vision. Cambridge university press, 2003.
- Yicong Hong, Kai Zhang, Jiuxiang Gu, Sai Bi, Yang Zhou, Difan Liu, Feng Liu, Kalyan Sunkavalli, Trung Bui, and Hao Tan. LRM: Large Reconstruction Model for Single Image to 3D. In International Conference on Learning Representations (ICLR), 2024.



- Tero Karras, Samuli Laine, and Timo Aila. A Style-Based Generator Architecture for Generative Adversarial Networks. In Proceedings of the IEEE/CVF conference on computer vision and pattern recognition (CVPR), pp. 4401–4410, 2019.
- Tero Karras, Samuli Laine, Miika Aittala, Janne Hellsten, Jaakko Lehtinen, and Timo Aila. Analyzing and Improving the Image Quality of StyleGAN. In Proceedings of the IEEE/CVF conference on computer vision and pattern recognition (CVPR), pp. 8110–8119, 2020.
- Bernhard Kerbl, Georgios Kopanas, Thomas Leimkuehler, and George Drettakis. 3D Gaussian Splatting for Real-Time Radiance Field Rendering. In ACM Transactions on Graphics (TOG), 2023.
- Diederik Kingma and Jimmy Ba. Adam: A Method for Stochastic Optimization. In International Conference on Learning Representations (ICLR), San Diego, CA, USA, 2015.
- Hongyang Li, Hao Zhang, Zhaoyang Zeng, Shilong Liu, Feng Li, Tianhe Ren, and Lei Zhang. DFA3D: 3D Deformable Attention For 2D-to-3D Feature Lifting. In Proceedings of the IEEE/CVF international conference on computer vision (ICCV), 2023a.
- Hongyang Li, Hao Zhang, Shilong Liu, Zhaoyang Zeng, Tianhe Ren, Feng Li, and Lei Zhang. TAPTR: Tracking Any Point with Transformers as Detection. In Proceedings of the IEEE/CVF European Conference on Computer Vision (ECCV), 2024.
- Jiahao Li, Hao Tan, Kai Zhang, Zexiang Xu, Fujun Luan, Yinghao Xu, Yicong Hong, Kalyan Sunkavalli, Greg Shakhnarovich, and Sai Bi. Instant3D: Fast Text-to-3D with Sparse-View Generation and Large Reconstruction Model. The International Conference on Learning Representations (ICLR), 2023b.
- Zhiqi Li, Wenhai Wang, Hongyang Li, Enze Xie, Chonghao Sima, Tong Lu, Yu Qiao, and Jifeng Dai. BEVFormer: Learning Bird’s-Eye-View Representation from Multi-Camera Images via Spatiotemporal Transformers. European conference on computer vision (ECCV), 2022.
- Kai-En Lin, Yen-Chen Lin, Wei-Sheng Lai, Tsung-Yi Lin, Yichang Shih, and Ravi Ramamoorthi. Vision Transformer for NeRF-Based View Synthesis from a Single Input Image. In 2023 IEEE/CVF Winter Conference on Applications of Computer Vision (WACV), 2022.
- Kenkun Liu, Derong Jin, Ailing Zeng, Xiaoguang Han, and Lei Zhang. A Comprehensive Benchmark for Neural Human Radiance Fields. Advances in Neural Information Processing Systems (NIPS), 36, 2024a.
- Minghua Liu, Ruoxi Shi, Linghao Chen, Zhuoyang Zhang, Chao Xu, Xinyue Wei, Hansheng Chen, Chong Zeng, Jiayuan Gu, and Hao Su. One-2-3-45++: Fast Single Image to 3D Objects with Consistent Multi-View Generation and 3D Diffusion. In Proceedings of the IEEE/CVF Conference on Computer Vision and Pattern Recognition, pp. 10072–10083, 2024b.
- Minghua Liu, Chao Xu, Haian Jin, Linghao Chen, Mukund Varma T, Zexiang Xu, and Hao Su. One-2-3-45: Any single image to 3d mesh in 45 seconds without per-shape optimization. In Conference on Neural Information Processing Systems (NIPS), 2024c.
- Minghua Liu, Chong Zeng, Xinyue Wei, Ruoxi Shi, Linghao Chen, Chao Xu, Mengqi Zhang, Zhaoning Wang, Xiaoshuai Zhang, Isabella Liu, Hongzhi Wu, and Hao Su. Meshformer: High-quality mesh generation with 3d-guided reconstruction model. Conference on Neural Information Processing Systems (NIPS), 2024d.
- Ruoshi Liu, Rundi Wu, Basile Van Hoorick, Pavel Tokmakov, Sergey Zakharov, and Carl Vondrick. Zero-1-to-3: Zero-shot One Image to 3D Object. In IEEE/CVF International Conference on Computer Vision (ICCV), 2023a.
- Shilong Liu, Feng Li, Hao Zhang, Xiao Yang, Xianbiao Qi, Hang Su, Jun Zhu, and Lei Zhang. DAB-DETR: Dynamic anchor boxes are better queries for DETR. In International Conference on Learning Representations (ICLR), 2022.

- Siyi Liu, Tianhe Ren, Jia-Yu Chen, Zhaoyang Zeng, Hao Zhang, Feng Li, Hongyang Li, Jun Huang, Hang Su, Jun-Juan Zhu, and Lei Zhang. Stable-DINO: Detection Transformer with Stable Matching. In IEEE/CVF International Conference on Computer Vision (ICCV), 2023b.
- Ze Liu, Yutong Lin, Yue Cao, Han Hu, Yixuan Wei, Zheng Zhang, Stephen Lin, and Baining Guo. Swin Transformer: Hierarchical vision transformer using shifted windows. In Proceedings of the IEEE/CVF international conference on computer vision (ICCV), pp. 10012–10022, 2021.
- Ben Mildenhall, Pratul P. Srinivasan, Matthew Tancik, Jonathan T. Barron, Ravi Ramamoorthi, and Ren Ng. NeRF: Representing Scenes as Neural Radiance Fields for View Synthesis. In The European Conference on Computer Vision (ECCV), 2020.
- Thomas Müller, Alex Evans, Christoph Schied, and Alexander Keller. Instant Neural Graphics Primitives with a Multiresolution Hash Encoding. In ACM Transactions on Graphics (SIGGRAPH), 2022.
- Sharan Narang, Gregory Diamos, Erich Elsen, Paulius Micikevicius, Jonah Alben, David Garcia, Boris Ginsburg, Michael Houston, Oleksii Kuchaiev, Ganesh Venkatesh, et al. Mixed Precision Training. In 6th international conference on learning representations (ICLR), volume 1, pp. 14, 2018.
- Charles R Qi, Hao Su, Kaichun Mo, and Leonidas J Guibas. PointNet: Deep Learning on Point Sets for 3D Classification and Segmentation. In Proceedings of the IEEE conference on computer vision and pattern recognition (CVPR), pp. 652–660, 2017a.
- Charles Ruizhongtai Qi, Li Yi, Hao Su, and Leonidas J Guibas. PointNet++: Deep Hierarchical Feature Learning on Point Sets in a Metric Space. Advances in neural information processing systems (NIPS), 30, 2017b.
- Robin Rombach, Andreas Blattmann, Dominik Lorenz, Patrick Esser, and Björn Ommer. High-resolution image synthesis with latent diffusion models. In Proceedings of the IEEE/CVF conference on computer vision and pattern recognition (CVPR), pp. 10684–10695, 2022.
- Olaf Ronneberger, Philipp Fischer, and Thomas Brox. U-Net: Convolutional Networks for Biomedical Image Segmentation. In Medical image computing and computer-assisted intervention (MICCAI), 2015.
- QiuHong Shen, Zike Wu, Xuanyu Yi, Pan Zhou, Hanwang Zhang, Shuicheng Yan, and Xinchao Wang. Gamba: Marry gaussian splatting with mamba for single view 3d reconstruction. arXiv preprint arXiv:2403.18795, 2024.
- Yichun Shi, Peng Wang, Jianglong Ye, Long Mai, Kejie Li, and Xiao Yang. MVDream: Multi-view Diffusion for 3D Generation. The International Conference on Learning Representations (ICLR), 2024.
- Jiaming Song, Chenlin Meng, and Stefano Ermon. Denoising Diffusion Implicit Models. In International Conference on Learning Representations (ICLR), 2021a.
- Yang Song, Jascha Sohl-Dickstein, Diederik P Kingma, Abhishek Kumar, Stefano Ermon, and Ben Poole. Score-Based Generative Modeling through Stochastic Differential Equations. The International Conference on Learning Representations (ICLR), 2021b. URL <https://openreview.net/forum?id=PxtTIG12RRHS>.
- Stanislaw Szymanowicz, Christian Rupprecht, and Andrea Vedaldi. Splatter Image: Ultra-Fast Single-View 3D Reconstruction. In IEEE/CVF Conference on Computer Vision and Pattern Recognition (CVPR), 2024.
- Jiaxiang Tang, Zhaoxi Chen, Xiaokang Chen, Tengfei Wang, Gang Zeng, and Ziwei Liu. LGM: Large Multi-View Gaussian Model for High-Resolution 3D Content Creation. In European Conference on Computer Vision, pp. 1–18. Springer, 2024a.
- Jiaxiang Tang, Jiawei Ren, Hang Zhou, Ziwei Liu, and Gang Zeng. DreamGaussian: Generative Gaussian Splatting for Efficient 3D Content Creation. In International Conference on Learning Representations (ICLR), 2024b.

- Dmitry Tochilkin, David Pankratz, Zexiang Liu, Zixuan Huang, , Adam Letts, Yangguang Li, Ding Liang, Christian Laforte, Varun Jampani, and Yan-Pei Cao. TripoSR: Fast 3D Object Reconstruction from a Single Image. arXiv preprint arXiv:2403.02151, 2024.
- Yuri Viazovetskyi, Vladimir Ivashkin, and Evgeny Kashin. StyleGAN2 Distillation for Feed-forward Image Manipulation. In Proceedings of the IEEE/CVF European Conference on Computer Vision (ECCV), pp. 170–186. Springer, 2020.
- Peng Wang and Yichun Shi. ImageDream: Image-Prompt Multi-view Diffusion for 3D Generation. arXiv preprint arXiv:2312.02201, 2023.
- Qianqian Wang, Zhicheng Wang, Kyle Genova, Pratul Srinivasan, Howard Zhou, Jonathan T. Barron, Ricardo Martin-Brualla, Noah Snavely, and Thomas Funkhouser. IBRNet: Learning Multi-View Image-Based Rendering. In 2021 IEEE/CVF Conference on Computer Vision and Pattern Recognition (CVPR), Jun 2021a. doi: 10.1109/cvpr46437.2021.00466. URL <http://dx.doi.org/10.1109/cvpr46437.2021.00466>.
- Wenhai Wang, Enze Xie, Xiang Li, Deng-Ping Fan, Kaitao Song, Ding Liang, Tong Lu, Ping Luo, and Ling Shao. Pyramid vision transformer: A versatile backbone for dense prediction without convolutions. In Proceedings of the IEEE/CVF international conference on computer vision (ICCV), pp. 568–578, 2021b.
- Zhou Wang, Alan C Bovik, Hamid R Sheikh, and Eero P Simoncelli. Image Quality Assessment: From Error Visibility to Structural Similarity. IEEE transactions on image processing, 13(4): 600–612, 2004.
- Xinyue Wei, Kai Zhang, Sai Bi, Hao Tan, Fujun Luan, Valentin Deschaintre, Kalyan Sunkavalli, Hao Su, and Zexiang Xu. Meshlrn: Large reconstruction model for high-quality mesh. arXiv preprint arXiv:2404.12385, 2024.
- Jiamin Wu, Kenkun Liu, Han Gao, Xiaoke Jiang, and Lei Zhang. DIG3D: Marrying Gaussian Splatting with Deformable Transformer for Single Image 3D Reconstruction. arXiv preprint arXiv:2404.16323, 2024.
- Zhangyang Xiong, Chenghong Li, Kenkun Liu, Hongjie Liao, Jianqiao Hu, Junyi Zhu, Shuliang Ning, Lingteng Qiu, Chongjie Wang, Shijie Wang, et al. MVHumanNet: A Large-scale Dataset of Multi-view Daily Dressing Human Captures. In Proceedings of the IEEE/CVF Conference on Computer Vision and Pattern Recognition (CVPR), pp. 19801–19811, 2024.
- Jiale Xu, Weihao Cheng, Yiming Gao, Xintao Wang, Shenghua Gao, and Ying Shan. InstantMesh: Efficient 3D Mesh Generation from a Single Image with Sparse-view Large Reconstruction Models. arXiv preprint arXiv:2404.07191, 2024.
- Jiayu Yang, Ziang Cheng, Yunfei Duan, Pan Ji, and Hongdong Li. ConsistNet: Enforcing 3D Consistency for Multi-view Images Diffusion. In Proceedings of the IEEE/CVF Conference on Computer Vision and Pattern Recognition (CVPR), pp. 7079–7088, 2024.
- Xuanyu Yi, Zike Wu, Qiuhong Shen, Qingshan Xu, Pan Zhou, Joo-Hwee Lim, Shuicheng Yan, Xinchao Wang, and Hanwang Zhang. MVGamba: Unify 3D Content Generation as State Space Sequence Modeling. arXiv preprint arXiv:2406.06367, 2024.
- Alex Yu, Vickie Ye, Matthew Tancik, and Angjoo Kanazawa. pixelNeRF: Neural Radiance Fields from One or Few Images. In IEEE/CVF Conference on Computer Vision and Pattern Recognition (CVPR), 2021.
- Hao Zhang, Feng Li, Shilong Liu, Lei Zhang, Hang Su, Jun-Juan Zhu, Lionel Ming shuan Ni, and Heung yeung Shum. DINO: DETR with Improved DeNoising Anchor Boxes for End-to-End Object Detection. In The International Conference on Learning Representations (ICLR), 2023.
- Kai Zhang, Sai Bi, Hao Tan, Yuanbo Xiangli, Nanxuan Zhao, Kalyan Sunkavalli, and Zexiang Xu. GS-LRM: Large Reconstruction Model for 3D Gaussian Splatting. European Conference on Computer Vision, 2024.

- Richard Zhang, Phillip Isola, Alexei A. Efros, Eli Shechtman, and Oliver Wang. The Unreasonable Effectiveness of Deep Features as a Perceptual Metric. In IEEE/CVF Conference on Computer Vision and Pattern Recognition (CVPR), 2018a.
- Richard Zhang, Phillip Isola, Alexei A. Efros, Eli Shechtman, and Oliver Wang. The Unreasonable Effectiveness of Deep Features as a Perceptual Metric. In Proceedings of the IEEE conference on computer vision and pattern recognition (CVPR), pp. 586–595, 2018b.
- Chuanxia Zheng and Andrea Vedaldi. Free3D: Consistent Novel View Synthesis without 3D Representation. In IEEE/CVF Conference on Computer Vision and Pattern Recognition (CVPR), 2024.
- Xizhou Zhu, Weijie Su, Lewei Lu, Bin Li, Xiaogang Wang, and Jifeng Dai. Deformable DETR: Deformable Transformers for End-to-End Object Detection. In The International Conference on Learning Representations (ICLR), 2021.
- Zi-Xin Zou, Zhipeng Yu, Yuan-Chen Guo, Yangguang Li, Ding Liang, Yan-Pei Cao, and Song-Hai Zhang. Triplane Meets Gaussian Splatting: Fast and Generalizable Single-View 3D Reconstruction with Transformers. In Proceedings of the IEEE/CVF Conference on Computer Vision and Pattern Recognition (CVPR), pp. 10324–10335, June 2024.
- M. Zwicker, H. Pfister, J. van Baar, and M. Gross. EWA volume splatting. In IEEE Visualization (IEEE VIS), 2001.

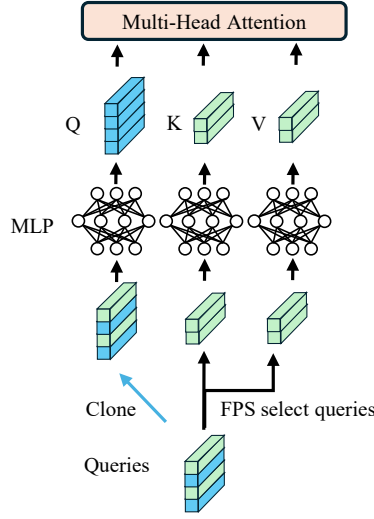


**Figure 6:** Spatially Efficient Self-Attention: While employing all queries as query in the self-attention mechanism, we leverage Farthest Point Sampling (FPS) to downsample certain 3D Gaussians. This process enables the extraction of their corresponding queries as keys and values within the self-attention operation.

## A APPENDIX

### A.1 SPATIAL EFFICIENT SELF ATTENTION (SESA)

While our 3D-aware deformable attention mechanism is notably efficient, the computational cost and memory occupation mainly arises in the self-attention component, particularly when dealing with a large number of 3D Gaussians. However, updating each 3D Gaussian with information from all others is not always necessary because those neighbouring 3D Gaussians usually carry similar information.

To mitigate this issue, as depicted in fig. 6 and drawing inspiration from Wang et al. (2021b), we introduce a technique aimed at reducing the size of the key and value components while maintaining the query component unaltered within the self-attention process. The core concept behind this approach is that while each 3D Gaussian requires updating, not every other 3D Gaussian needs to contribute to this update. We achieve this by selectively updating each query solely with a subset of corresponding queries linked to other 3D Gaussians.

To retain crucial information flow, we leverage the Fast Point Sampling (FPS) algorithm commonly used in point cloud methodologies like PointNet (Qi et al., 2017a) and PointNet++ (Qi et al., 2017b). Specifically, we employ the Gaussian centers  $\mu$  to identify the most distantly located points and use these points to index the queries. By implementing this strategy, we significantly reduce the model’s overall memory footprint while preserving essential information exchange among the Gaussians.

### A.2 IMPLEMENTATION DETAILS

**Dataset** We utilized a refined subset of the Objaverse LVIS dataset (Deitke et al., 2023) for both training and validating our model. This subset was curated to exclude low-quality models, resulting in a dataset containing 36,044 high-quality objects. This open-category dataset encompasses a diverse range of objects commonly encountered in everyday scenarios. For training, we leveraged rendered images provided by zero-1-to-3 (Liu et al., 2023a) for the random input setting. Each object in the dataset is associated with approximately 12 random views, accompanied by their respective camera poses. We partitioned 99% of the objects for training purposes, reserving the remaining 1% for validation. During training, we randomly selected a subset of views as input while using all 12 views for supervision. Each rendered image has a resolution of  $512 \times 512$ , which we downsampled to

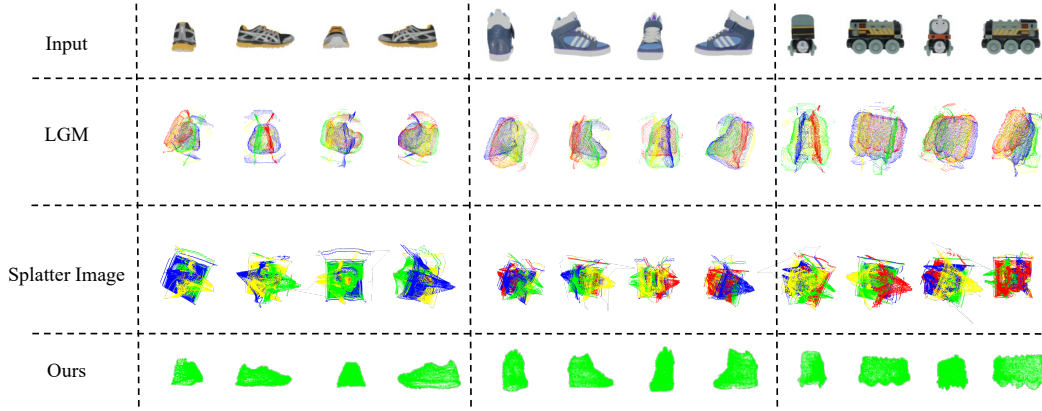


**Figure 7:** Point clouds of the center of Gaussians from each view. The Gaussians from different views are in different colors.

$128 \times 128$ . For the fixed view setting, we render the images with fixed views as input and 32 more random views with elevation in  $(-30, 30)$  degrees for supervision.

To evaluate our model’s performance in open-category settings, we conducted tests on the Google Scanned Objects (GSO) benchmark (Downs et al., 2022). The GSO dataset comprises 1,030 3D objects categorized into 17 classes. For this evaluation, we utilized rendered images sourced from Free3D (Zheng & Vedaldi, 2024), which consist of 25 random views along with their corresponding camera poses. Notably, there are no restrictions on the elevation of the rendered views. We utilized the initial views as inputs and the remaining views for assessing our novel view synthesis task. Additionally, we observed that LGM (Tang et al., 2024a) only support fixed-view inputs (e.g., front, left, back, and right). To address this, we evaluated a new rendered GSO dataset at 0 degrees elevation, testing it on 32 random views with elevations ranging from 0 to 30 degrees. To distinguish between the two test sets, we refer to them as GSO-random and GSO-fixed respectively in the following analysis.

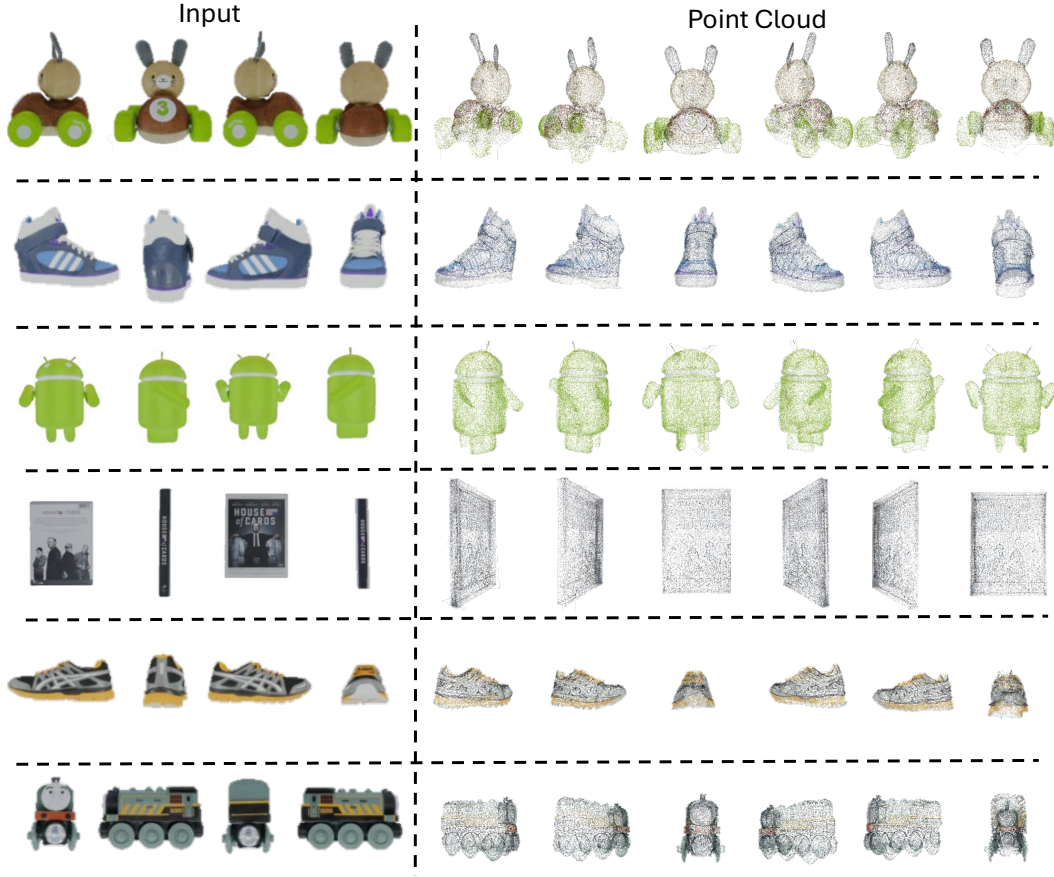
**Experiment setting** We train our model on the setting of 4 views, each time we randomly select 4 views as input and all the views for supervision. In the coarse stage, we train the model with less views (i.e. 2 views) with resolution  $128 \times 128$  and generate 16384 3D Gaussians as initialization of the fine stage. In the fine stage, We use 19600 3D Gaussians to represent the 3D object. For the 3D Gaussians from the coarse stage, we use the mask to remove the background points and padding the number of 3D Gaussians to 19600 by copying some of the remaining 3D Gaussians. The selected 3D Gaussians are then utilized to project queries onto image plane in the refine stage. In each deformable attention layer, we utilize 4 sampling points for each projected 3D Gaussian reference point to sample values on the image.

We use 4 decoder layers and the hidden dimension is 256. Moreover, when training the fine stage, we finetune both the coarse stage and the encoder. We use a mixed-precision training (Narang et al., 2018) with BF16 data type. We train our model with Adam (Kingma & Ba, 2015) optimizer and the learning rate is 0.0001. We take 300K iteration with batch size 4. For the coarse stage, we train it on 8 3090 GPUs (24G) for 5 days and for the fine stage, we train it on 8 A100 (80G) for 3 days.

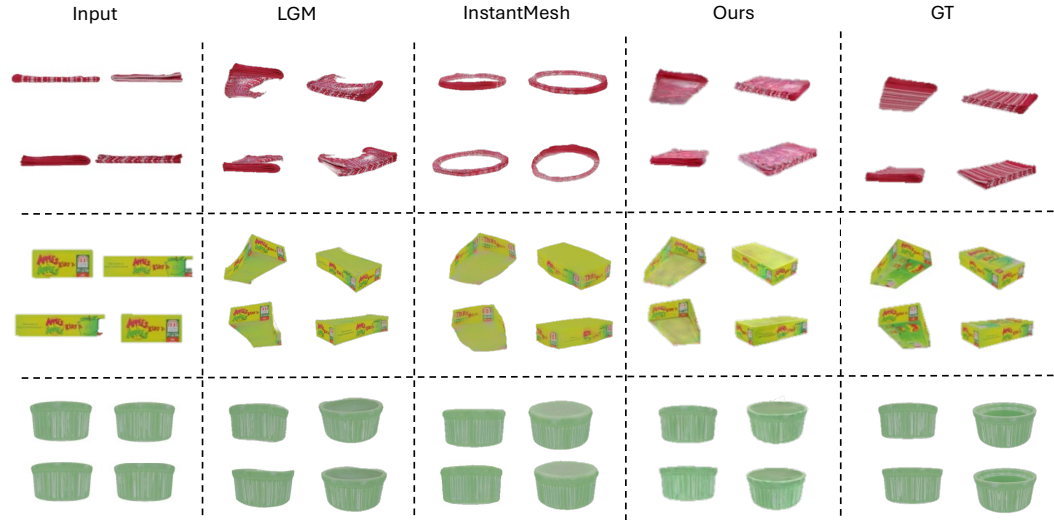
### A.3 MORE RESULTS

#### A.3.1 QUALITY RESULTS

**View consistency problem** We gives more view inconsistency visualization problem by visualize center of Gaussians from each view in different colors, as shown in fig. 7. Gaussians from different views representing the same part of the object may lays on the different position in the 3D space and thus cause the view inconsistency problem.



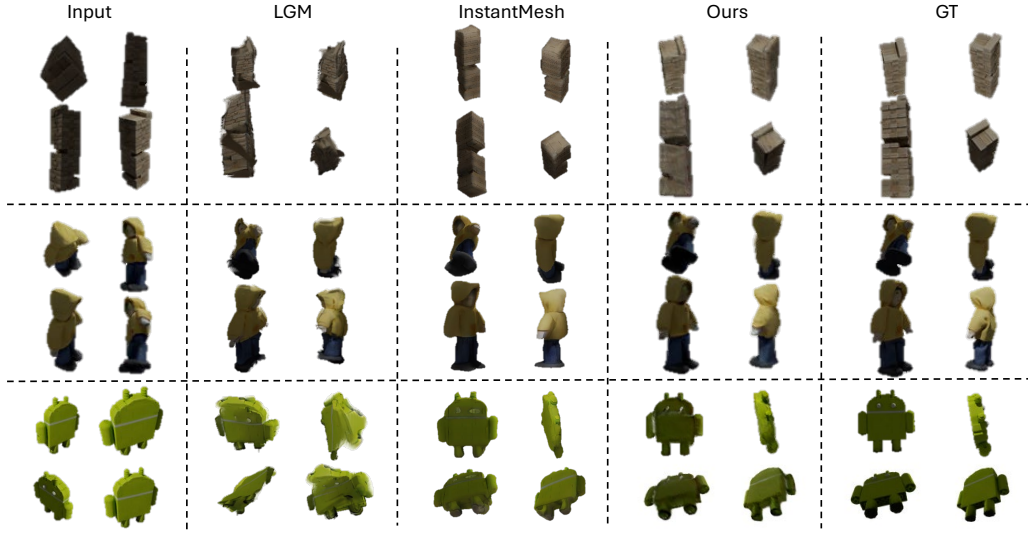
**Figure 8:** 3D Gaussian center as point cloud on GSO-fixed dataset for inputting 4 views.



**Figure 9:** Quality for rendered novel views on GSO-fixed dataset for inputting 4 views with resolution 256 LGM large model.

**More visualization** We show the point cloud visualization in fig. 8 underscores our model’s ability to capture geometry effectively, not just rendering quality.

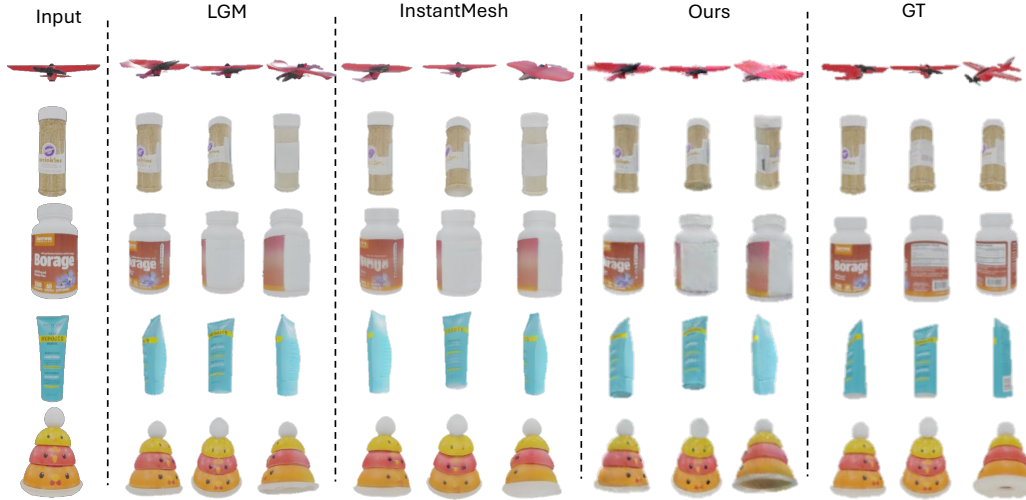




**Figure 10:** Quality for rendered novel views on GSO-random dataset for inputting 4 views.

As shown in fig. 9, when given limited number of input, neither LGM nor InstantMesh gives the meaningful geomery.

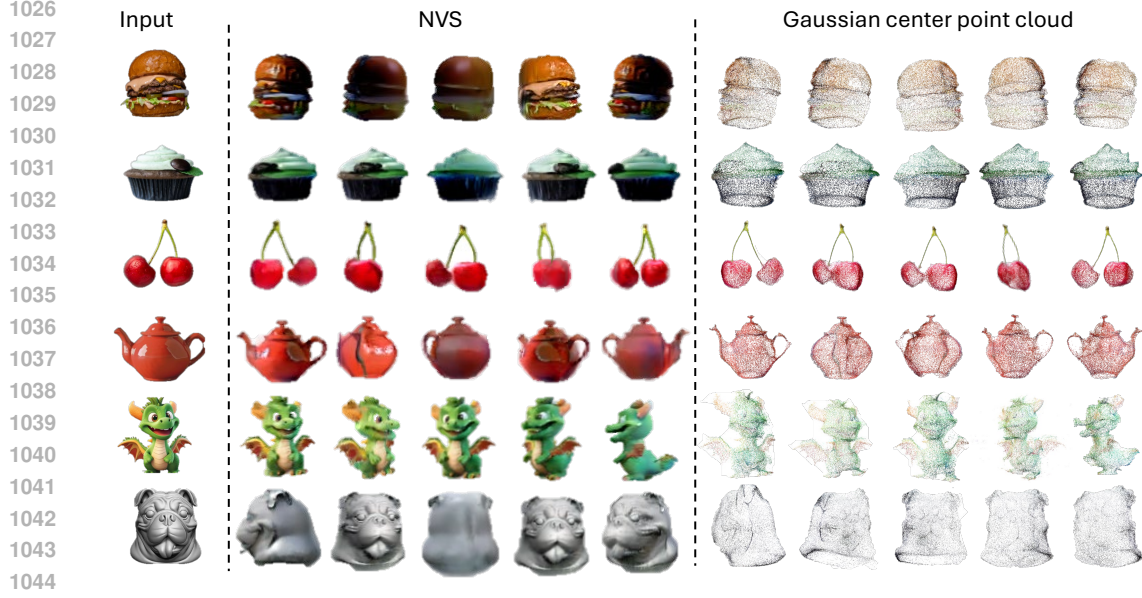
fig. 10 presents the quantitative results of novel views rendered by recent models trained on 4 views. When provided with 4 random views as input, LGM (Tang et al., 2024a) demonstrates a loss of geometry and encounters view inconsistency problems stemming from its training on fixed views. In contrast, our approach produces a cohesive 3D Gaussian set that effectively captures object geometries.



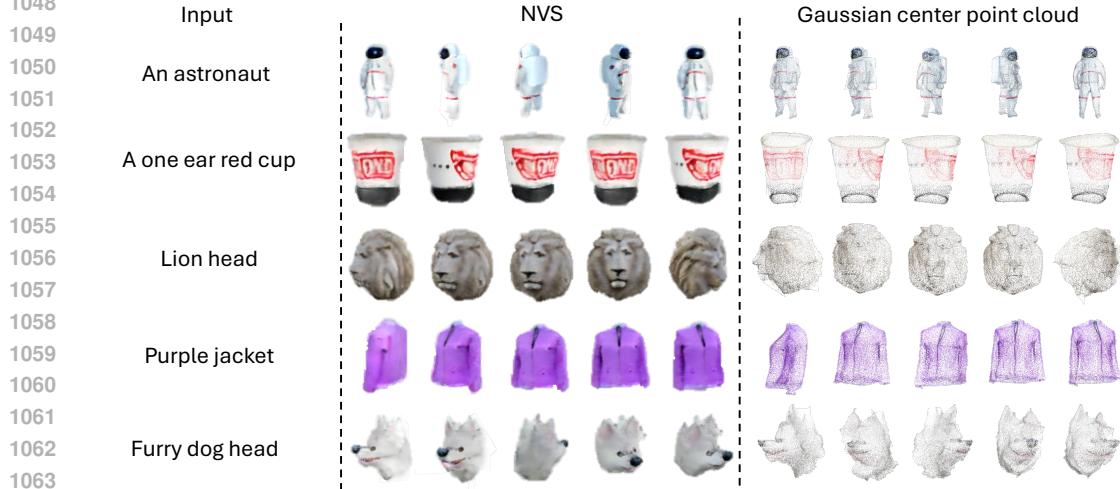
**Figure 11:** Quality for rendered novel views on GSO dataset for inputting 1 view and using Image-Fusion to generate 4 views.

fig. 11 and fig. 12, respectively. The figures illustrate that LGM encounters the issue of view inconsistency; for instance, there are multiple handles visible for the mushroom teapot. InstantMesh loses some details due to its utilization of a discrete triplane to represent continuous 3D space.

fig. 13 shows the result of text-to-3D task. We have incorporated text-to-3D capabilities into our model. To assess quality, we employ MVDream (Shi et al., 2024) to create a single image from a



**Figure 12:** Quality for rendered novel views on in the wild data for inputting 1 view and using ImageDream to generate 4 views.



**Figure 13:** Quality for rendered novel views on inputting text and using MVDream to generate 4 views.

text prompt. Subsequently, a diffusion model is utilized to generate multi-view images, which are then processed by our model to obtain a 3D representation.

The setting of random input view is obvious a more challenging task than the setting of fixed input view, thus our method also inevitably suffers from a performance drop but still perform better than other state-of-the-art methods. As for Splatter Image (Szymanowicz et al., 2024), it also meets a significant performance drop when random input views are used as its SSIM  $\uparrow$  decreased from 0.9151 to 0.8932 and LPIPS  $\downarrow$  increased from 0.1517 to 0.2575 despite its PSNR  $\uparrow$  has a slight increase. We visualize the results of the two settings to show the difference in fig. 14.

### A.3.2 QUANTITY RESULTS

**Splatter Image visualization** PSNR of Splatter Image in table 2 is good but SSIM and LPIPS are not good enough, we further provide the visualization in fig. 15.

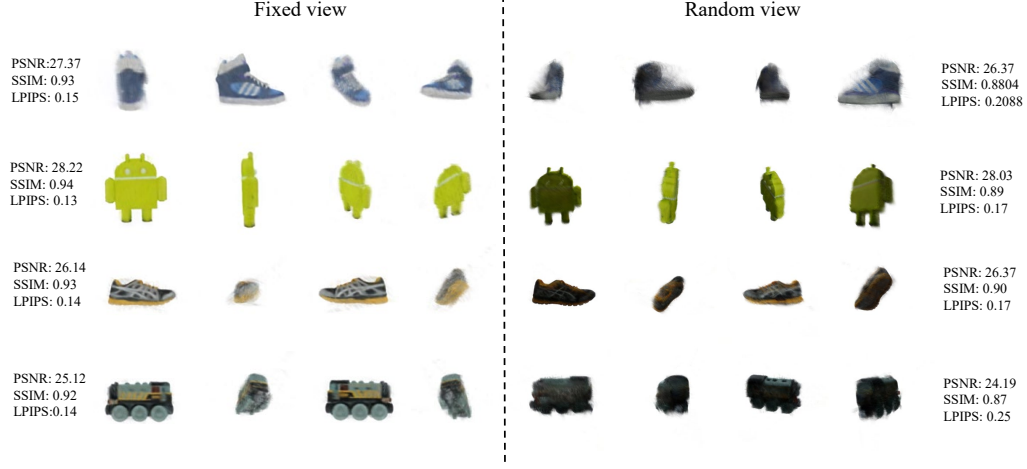


**Figure 14:** Visualization for Splatter Image with fixed view input and random view input.

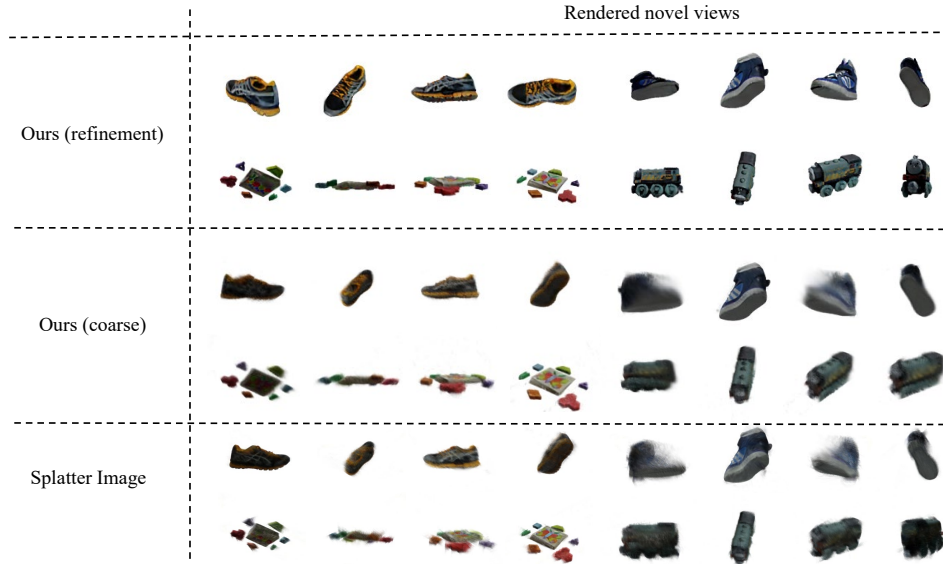


**Figure 15:** Visualization for Splatter Image with fixed view input and random view input.

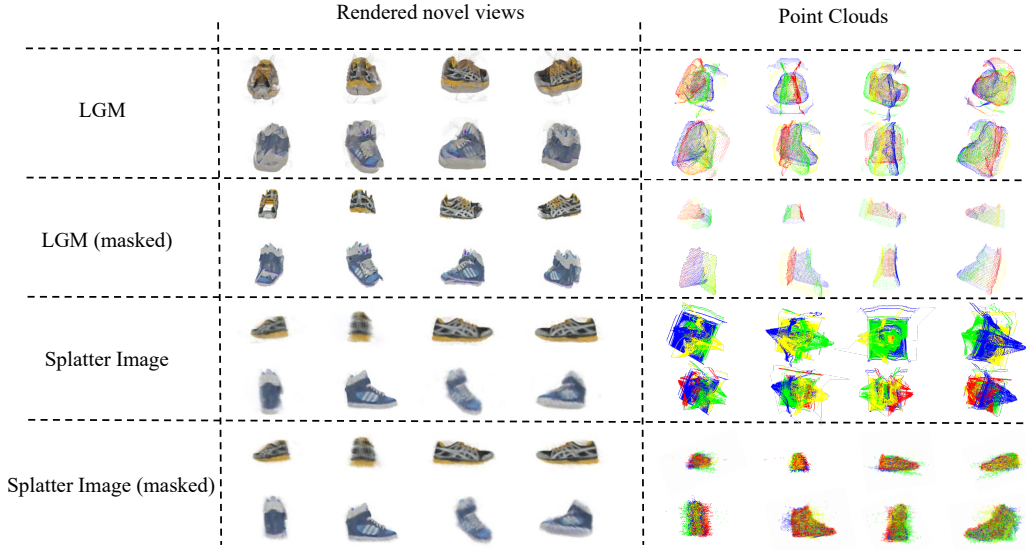
**Figure 16:** Removing the background use mask for Splatter Image and LGM

Table 5: Quantitative results trained on Objaverse LVIS and tested on GSO. 3D sup. means need 3D supervision.

Method	PSNR $\uparrow$	SSIM $\uparrow$	LPIPS $\downarrow$	3D sup.	Inference time
Triplane-Gaussian (Zou et al., 2024)	18.61	0.853	0.159	✓	1.906
Ours	<b>23.45</b>	<b>0.897</b>	<b>0.093</b>	✗	<b>0.476</b>

**Single image reconstruction** There are common points between our model and TriplaneGaussian and Instant3D that we all use a unitary representation and use Transformer to regress. For Instant3D, it transforms image to Nerf, making longer rendering time. For Triplane Gaussian, which is a single view reconstruction model with complex and costly triplane representation, representing compresses 3D space, leading to a lack of detailed information in the 3D structure and imposing a rigid grid alignment that limits flexibility (Tang et al., 2024a; Qi et al., 2017a). In the contrast, we use a more efficient way (deformable attention) to decode Gaussians. The comparison between Triplane-Gaussian and our methods is shown in table 5. Triplane Gaussian requires 3D supervision and takes longer inference time while get worse performance comparing to our model. We test on the given light-weight checkpoint in the github on the single view situation.

Table 6: Comparison between masked and original pixel aligned methods

Method	PSNR $\uparrow$	SSIM $\uparrow$	LPIPS $\downarrow$
LGM	17.4810	0.7829	0.2180
LGM (masked)	21.6008	0.8608	0.1232
Splatter Image	25.6241	0.9151	0.1517
Splatter Image (masked)	25.0648	0.9147	0.1684

**Comparison to masked LGM and Splatter Image** To better explain that the view inconsistency problem is not caused by the background points from previous methods, we provide the results on removing background points of LGM and Splatter Image. LGM uses mask loss to make the most of the pixels contribute to the object itself, even for the background pixels, therefore, removing background use mask makes the results more sparse. It also removing some outliers and thus the rendering results is better as shown in table 6. Splatter Image keep most of the pixels contribute to its original position, making most of the background points still located on a plane instead of the object. Therefore, removing background use mask does not influence the rendering result much

but the rendering quality still reduced a little. Moreover, the view-inconsistency is not caused by the background points but the mis-alignment of 3D Gaussians from different views, removing the background use mask does not help solving the problem. We show the visualization in fig. 16

**Other number of view results** We present the results of training with varying numbers of views (2, 6, 8) and evaluate the corresponding results with the same number of views in table 7.

Table 7: Quantitative results of novel view synthesis training using 2, 6, and 8 input views, tested on the GSO-random dataset across 2, 6, and 8 views.

Method	2 views			6 views			8 views		
	PSNR $\uparrow$	SSIM $\uparrow$	LPIPS $\downarrow$	PSNR $\uparrow$	SSIM $\uparrow$	LPIPS $\downarrow$	PSNR $\uparrow$	SSIM $\uparrow$	LPIPS $\downarrow$
Splatter Image	22.6390	0.8889	0.1569	26.1225	0.9178	0.1620	26.4588	0.9166	0.1714
Our Model	<b>23.8384</b>	<b>0.8995</b>	<b>0.1254</b>	<b>28.1035</b>	<b>0.9489</b>	<b>0.0559</b>	<b>28.8262</b>	<b>0.9537</b>	<b>0.0492</b>

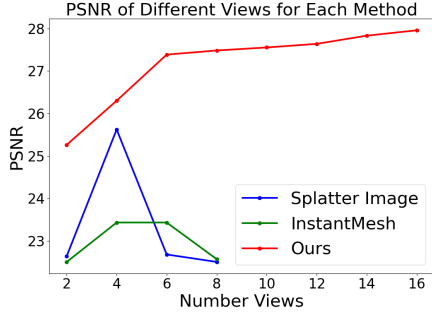


Figure 17: Visualization for Splatter Image with fixed view input and random view input.

InstantMesh (Tang et al., 2024a; Xu et al., 2024), we first leverage a multi-view diffusion model, ImageDream (Wang & Shi, 2023), to generate four predetermined views. Subsequently, our model is employed for 3D Gaussian reconstruction. A comparative analysis with LGM and InstantMesh is detailed in table 8. For this particular scenario, we utilize the fixed-view GSO test set with elevations ranging between 0 and 30 degrees. Given potential variations in camera poses among the generated multi-views, which may not align precisely with standard front, right, back, and left perspectives, we selectively retain 266 objects that consistently yield accurate images under the provided camera poses.

Table 8: Quantitative results for single view reconstruction on GSO dataset.

Method	PSNR $\uparrow$	SSIM $\uparrow$	LPIPS $\downarrow$
LGM (Tang et al., 2024a)	20.8139	0.8581	0.1508
InstantMesh (Xu et al., 2024)	19.4667	0.8379	0.1842
Our Model	<b>22.3534</b>	<b>0.8567</b>	<b>0.1492</b>

#### A.4 ABLATION STUDY

**Number of views in the coarse stage** We add the ablation study on the number of images used during the coarse stage here. The results shown is that the number of images used during the coarse stage does not influence the final result. The reason that we choose the number of views being 2 is that we want to support any number of input views. For example, if we choose the number of views in the coarse stage being 8, we should at least provide 8 views so that the model can not support the

Our model is positioned on the ‘sparse view’ setting, which indicates the number of views less than 10, so we only reports the performance of views from 2 to 8 in the main paper. With the increase of input views, information from similar views becomes redundant, so the gain for our model has become plateaued while other methods suffer from performance drop as they cannot handle too many input views due to the view inconsistent problem. As we keep increasing the number of input views larger than 8, our method can still benefit from more input views (as shown in fig. 17) while others meet the CUDA-out-of-memory problem.

**Image-to-3D** Image-to-3D conversion represents a fundamental application in 3D generation. Following the methodology of LGM and



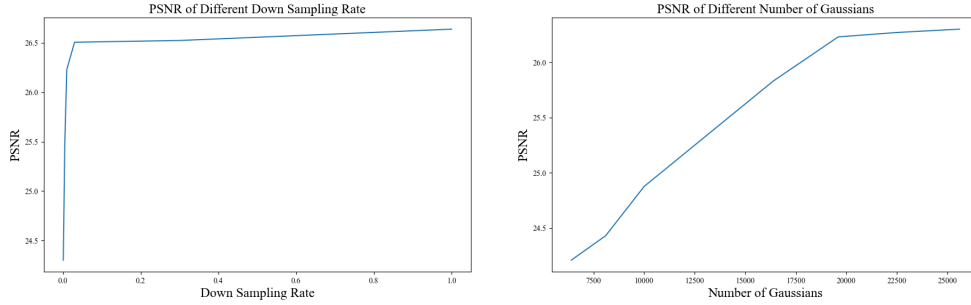


**Figure 18:** Left: PSNR with different down sampling rate in the spatial efficient self attention. Right: PSNR with different number of Gaussians.

number of views smaller than 8. And we tried to change the input views but the number of input views keeping 2 unchanged, the variance of PSNR for 10 different experiments is within 0.185.

Table 9: Ablation study results of different view and different number of views for the coarse stage (with 4 views in the refinement stage)

Number of views in coarse stage	PSNR $\uparrow$	SSIM $\uparrow$	LPIPS $\downarrow$
1	30.2312	0.9608	0.0413
2	30.4245	0.9614	0.0422
3	30.3442	0.9618	0.0419
4	30.4521	0.9620	0.0412

**Convergence for different regression target** Upon investigation, we observe that prior techniques frequently predict depth rather than the centers of Gaussians. In our exploration, we conduct experiments focusing on regressing the centers of 3D Gaussians while keeping other aspects constant. Through this analysis, we discover that regressing the positions of 3D Gaussians can introduce convergence obstacles. Table 10 illustrates the outcomes of these experiments on the Objaverse validation dataset after 100K steps.

Table 10: Ablation study on parameter selection.

Regression target	PSNR $\uparrow$	SSIM $\uparrow$	LPIPS $\downarrow$
Depth	24.3792	0.9012	0.1014
3D Gaussian centers (random initialize in visual cone)	19.2551	0.8343	0.1876
Coarse-to-fine	<b>25.5338</b>	<b>0.9126</b>	<b>0.0833</b>

**More ablation studies** Here we gives more ablation study mainly for hyperparameter selection. Due to computational costs, ablation models are trained at 100k iteration and test on Objaverse validation dataset.

**Hyperparameter selection** As previously highlighted, the memory bottleneck of our model lies in the pointwise self-attention mechanism. To address this, we implement a spatially efficient self-attention technique to alleviate memory consumption. Illustrated in fig. 18 (left), as we augment the downsampling rate of the key and value in the self-attention mechanism, the memory overhead diminishes linearly, while the PSNR reduction is not as rapid. Consequently, we opt for a down-sampling rate located at the inflection point, which we determine to be 0.01, balancing memory efficiency with reconstruction quality. Similarly, we select the number of Gaussians as 19600 as shown in fig. 18 (right).

In table 11, we opted for 4 decoder layers over 6, as the latter offers marginal improvement but demands significantly more computational resources. Additionally, we experimented with using the

Table 11: Ablation study on parameter selection.

Method	PSNR $\uparrow$	SSIM $\uparrow$	LPIPS $\downarrow$
2 decoder layers	24.5229	0.9195	0.1021
6 decoder layers	<b>26.2442</b>	<b>0.9352</b>	<b>0.0778</b>
Freeze coarse stage finetune encoder	25.6902	0.9223	0.0826
Freeze both coarse stage and encoder	25.3211	0.9264	0.1003
Default model	26.2313	0.9351	0.0788

fine stage initialized with the coarse stage as the encoder and tested the efficacy of fine-tuning both stages. Our findings indicate that fine-tuning both stages yields the best results.